A transcriptionally and functionally distinct PD-1+ CD8+ T cell pool with predictive potential in non-small-cell lung cancer treated with PD-1 blockade

Thommen, Daniela S ; Koelzer, Viktor H ; Herzig, Petra ; Roller, Andreas ; Trefny, Marcel ; Dimeloe, Sarah ; Kiialainen, Anna ; Hanhart, Jonathan ; Schill, Catherine ; Hess, Christoph ; Savic Prince, Spasenija ; Wiese, Mark ; Lardinois, Didier ; Ho, Ping-Chih ; Klein, Christian ; Karanikas, Vaios ; Mertz, Kirsten D ; Schumacher, Ton N ; Zippelius, Alfred

Abstract: Evidence from mouse chronic viral infection models suggests that CD8+ T cell subsets characterized by distinct expression levels of the receptor PD-1 diverge in their state of exhaustion and potential for reinvigoration by PD-1 blockade. However, it remains unknown whether T cells in human cancer adopt a similar spectrum of exhausted states based on PD-1 expression levels. We compared transcriptional, metabolic and functional signatures of intratumoral CD8+ T lymphocyte populations with high (PD-1T), intermediate (PD-1N) and no PD-1 expression (PD-1–) from non-small-cell lung cancer patients. PD-1T T cells showed a markedly different transcriptional and metabolic profile from PD-1N and PD-1– lymphocytes, as well as an intrinsically high capacity for tumor recognition. Furthermore, while PD-1T lymphocytes were impaired in classical effector cytokine production, they produced CXCL13, which mediates immune cell recruitment to tertiary lymphoid structures. Strikingly, the presence of PD-1T cells was strongly predictive for both response and survival in a small cohort of non-small-cell lung cancer patients treated with PD-1 blockade. The characterization of a distinct state of tumor-reactive, PD-1-bright lymphocytes in human cancer, which only partially resembles that seen in chronic infection, provides potential avenues for therapeutic intervention.

DOI: https://doi.org/10.1038/s41591-018-0057-z

Published in final edited form as:
Nat Med. 2018 July ; 24(7): 994–1004. doi:10.1038/s41591-018-0057-z.

A transcriptionally and functionally distinct PD-1^{+} CD8^{+} T cell pool with predictive potential in non-small cell lung cancer treated with PD-1 blockade

D.S. Thommen[1,2], **V.H. Koelzer**[#3,4], **P. Herzig**[#1], **A. Roller**[#5], **M. Trefny**[1], **S. Dimeloe**[6], **A. Kiialainen**[5], **J. Hanhart**[3], **C. Schill**[7], **C. Hess**[6], **S. Savic Prince**[8], **M. Wiese**[9], **D. Lardinois**[9], **P.C. Ho**[10], **C. Klein**[11], **V. Karanikas**[11], **K.D. Mertz**[3], **T.N. Schumacher**[2,14], and **A. Zippelius**[1,12,14]

[1]Cancer Immunology, Department of Biomedicine, University Hospital Basel, Switzerland [2]Division of Molecular Oncology and Immunology, Oncode Institute, The Netherlands Cancer Institute, Amsterdam, The Netherlands [3]Institute of Pathology, Cantonal Hospital Baselland, Liestal, Switzerland [4]Molecular and Population Genetics Laboratory, University of Oxford, UK [5]Roche Pharmaceutical Research and Early Development, Roche Innovation Center Basel, Switzerland [6]Immunobiology, Department of Biomedicine, University Hospital Basel, Switzerland [7]Oncology, Cantonal Hospital Baselland, Liestal, Switzerland [8]Institute of Pathology, University Hospital Basel, Switzerland [9]Department of Surgery, University Hospital Basel, Switzerland [10]University of Lausanne, Ludwig Center for Cancer Research, Epalinges, Switzerland [11]Roche Pharmaceutical Research and Early Development, Roche Innovation Center Zurich, Switzerland [12]Medical Oncology, University Hospital Basel, Switzerland

Correspondence should be addressed to: D.S.T. (d.thommen@nki.nl) or A.Z. (alfred.zippelius@usb.ch).
[14]These authors jointly directed this work.

Life Sciences Reporting Summary.
Further information on experimental design and reagents are available in the Life Sciences Reporting Summary.

Data availability statement.
The data sets generated and/or analyzed during the current study are included within the supplementary information or have been deposited in Gene Expression Omnibus (RNA sequencing data) under accession code GSE99531. All other data are available from the corresponding authors upon reasonable request with exception of the PD-1^{T} predictive analysis.

Author contributions:
D.S.T.: study design and supervision, design and execution of the experiments; data acquisition, analysis and interpretation; writing and revision of the manuscript; V.H.K.: execution of immunohistochemistry stainings, digital image analysis; contribution to manuscript drafting and revision; P.H.: execution of experiments; contribution to manuscript drafting and revision; A.R.: statistical analysis and interpretation, contribution to manuscript drafting; M.T.: execution of experiments; A.K.: RNA-seq analysis; S.D.: design and technical support with metabolism analysis; J.H.: execution of immunohistochemistry and digital image analysis; C.S.: collection and analysis of clinical data; C.H.: design of metabolism experiments, contribution to manuscript drafting; S.S.P.: collection and pathological characterization of patient samples; M.W. and D.L.: recruitment and characterization of patients; P.C.H.: execution of experiments, contribution to manuscript drafting; C.K. and V.K.: contribution to manuscript drafting; K.D.M.: execution of immunohistochemistry analysis; contribution to manuscript drafting; T.N.S.: study design and supervision; writing and revision of the manuscript; A.Z.: study design and supervision, writing and revision of the manuscript.

Competing financial interests:
A.R., A.K., C.K., V.K. are employed by Roche. A.Z. received research funding from Roche. Part of the work described in this manuscript is the subject of a patent application co-owned by NKI-AVL and the University of Basel. Based on NKI-AVL and the University of Basel policy on management of intellectual property, D.S.T., V.H.K., K.D.M., A.Z. and T.N.S. would be entitled to a portion of received royalty income.

Europe PMC Funders Author Manuscripts

[#] These authors contributed equally to this work.

Abstract

Evidence from mouse chronic viral infection models suggests that $CD8^+$ T cell subsets characterized by distinct expression levels of the receptor PD-1 diverge in their state of exhaustion and potential for reinvigoration by PD-1 blockade. However, it remains unknown whether T cells in human cancer adopt a similar spectrum of exhausted states based on PD-1 expression levels. We compared transcriptional, metabolic, and functional signatures of intratumoral $CD8^+$ T lymphocyte populations with high ($PD\text{-}1^T$), intermediate ($PD\text{-}1^N$) and no PD-1 expression ($PD\text{-}1^-$) from non-small cell lung cancer patients. We observed that, $PD\text{-}1^T$ T cells show a markedly different transcriptional and metabolic profile as compared to $PD\text{-}1^N$ and $PD\text{-}1^-$ lymphocytes, as well as an intrinsically high capacity for tumor recognition. Furthermore, while $PD\text{-}1^T$ lymphocytes are impaired in classical effector cytokine production, they produce CXCL13 that mediates immune cell recruitment to tertiary lymphoid structures. Strikingly, the presence of $PD\text{-}1^T$ cells was strongly predictive for both response and survival in a small cohort of non-small cell lung cancer patients treated with PD-1 blockade. The characterization of a distinct state of tumor-reactive, PD-1 bright lymphocytes in human cancer, which only partially resembles that seen in chronic infection, provides novel potential avenues for therapeutic intervention.

Keywords

T cell exhaustion; NSCLC; chemokine; CXCL13; IL-10; immune checkpoint blockade

Introduction

Tumors with substantial amounts of DNA damage commonly induce tumor-reactive $CD8^+$ T cell responses in both mouse models and cancer patients[1,2]. Successful elimination of cancer cells by these tumor-infiltrating lymphocytes (TILs) is however hampered by a broad set of immunosuppressive mechanisms that are active in the tumor microenvironment (TME)[3–5], and this includes the upregulation of immune checkpoint proteins such as PD-1, CTLA-4, Tim-3 and Lag-3 on TILs[6]. T cells that express these checkpoint molecules are thought to be characterized by a state of dysfunction, termed T cell exhaustion, that was originally discovered in chronic murine lymphocytic choriomeningitis virus (LCMV) infection[7–9], but for which evidence has also been obtained in human infections and cancer[6,10–16]. The successful reinvigoration of T cell function by blockade of PD-1 or its ligand PD-L1 highlights the importance of this pathway in T cell exhaustion[10].

Notably, in chronic LCMV infection, two subsets of exhausted $PD\text{-}1^+$ T cells with distinct responses to PD-1/PD-L1 blockade have been identified. Specifically, whereas mouse T cells with high expression of the transcription factor T-bet and intermediate expression of PD-1 ($T\text{-}bet^{hi}$ $PD\text{-}1^{int}$) can be reinvigorated by *in vivo* blockade with anti-PD-L1, terminally differentiated T cells with high Eomesodermin (Eomes) and high PD-1 expression ($Eomes^{hi}$ $PD\text{-}1^{hi}$) do not respond[17,18]. Similarly, a high percentage of $PD\text{-}1^{hi}$ cells within $CD8^+$ TILs has been shown to correlate with a limited response to PD-1 blockade upon polyclonal stimulation of T cells in human lung cancer samples[14]. However, the relationship between

PD-1^{int} and PD-1^{hi} TILs in human cancer has not been established, and their resemblance to their counterparts in murine chronic infection has been unclear. To address these issues, we analyzed the properties of three populations of intratumoral CD8$^+$ TILs with defined levels of PD-1 expression in patients with non-small cell lung cancer (NSCLC): CD8$^+$ TILs without detectable PD-1 expression (PD-1$^-$), CD8$^+$ TILs with a PD-1 expression level similar to that on healthy donor PBMCs (PD-1^N), and CD8$^+$ TILs with levels of PD-1 that exceed those commonly observed on healthy donor PBMCs (PD-1^T). Using this approach, we evaluated (i) whether PD-1^T and PD-1^N characterize different cell states in human cancer, (ii) whether PD-1^T T cells in human cancer display the same defects as have been observed in murine chronic infection, and (iii) whether tumor reactivity is equally contained in the different PD-1 positive TIL subsets in human tumor lesions. Our data demonstrate that tumor reactivity is to a large extent restricted to the PD-1^T subset, and that these cells display a functional state that is distinct from that of both PD-1^N T cells in cancer and of PD-1^{hi} T cells in chronic infection, and characterized by high levels of CXCL13 production. Furthermore, the presence of PD-1^T TILs was highly predictive for response and survival upon anti-PD-1 treatment in NSCLC.

Results

PD-1 expression level identifies TIL subsets with distinct phenotype, function and tumor reactivity

To first understand whether the expression level of PD-1 can be used to identify tumor-infiltrating CD8$^+$ T cells that differ in the expression of other inhibitory receptors18–20, we determined the expression of Tim-3, Lag-3, TIGIT, 2B4 (CD244), and BTLA in nine subsets of CD8$^+$ TILs from 24 NSCLC specimens that were subdivided according to their PD-1 mean fluorescence intensity (MFI) (Fig. 1a and Supplementary Fig. 1a). For all inhibitory receptors, the percentage of expressing cells, but also the level of inhibitory receptor expression, was clearly correlated with PD-1 expression levels (Fig. 1b and Supplementary Fig. 1b-d). Whereas TIGIT and 2B4 were also expressed in T cells with intermediate and low PD-1 levels, Tim-3 and Lag-3 were almost exclusively found on lymphocytes with high levels of PD-1 expression. To establish a more objective subdivision of PD-1$^+$ populations that can be applied across studies, we compared the PD-1 expression levels on NSCLC TILs with those of peripheral blood T cells from healthy donors. In peripheral blood of healthy donors (n=6), a clear population of PD-1-negative T cells and T cells with an intermediate level of PD-1 could be detected, with very few T cells displaying higher levels of PD-1 (average of 0.4%). In contrast, in TILs, sometimes sizable populations of T cells with bright PD-1 expression were detected (fraction of PD-1 bright within CD8$^+$ TILs: 29.1±17.6%, n=24) (Fig. 1c and Supplementary Fig. 1e). Reflecting the definition of these cells on the basis of their tumor-associated level of PD-1 expression, we here refer to these cells as 'PD-1^T' ('tumor-associated') TILs. Remaining TILs were divided into those with a PD-1 level equal to that seen in peripheral blood ('PD-1^{Normal}, PD-1^N' TILs) and TILs with no detectable PD-1 expression ('PD-1$^-$' TIL, Fig. 1c).

As effector functions are gradually lost during progressive T cell exhaustion8, with a recent study reporting an inverse correlation between T cell function and PD-1 expression levels21,

we first assessed cytokine secretion by sorted PD-1^{T}, PD-1^{N} and PD-1^{-} TILs from three NSCLC samples (Supplementary Fig. 1f,g). Sorted cells were rested overnight and then stimulated using anti-CD3/anti-CD28 antibodies. While the PD-1^{N} and PD-1^{-} subsets produced all effector cytokines, PD-1^{T} TILs failed to produce substantial levels of IL-2, TNF-α and IFN-γ (Fig. 1d). Analysis of CD28 levels ruled out differential CD28 expression as a cause for this difference in responsiveness (Supplementary Fig. 1h).

Collectively, the above data were consistent with a model in which increasing exhaustion leads PD-1^{N} cells to convert to PD-1^{T} cells. To test this, we assessed two additional properties of these intratumoral T cell subsets. First, we assessed whether, as in chronic viral infection, the PD-1^{T} state was associated with the expression of Eomes and not T-bet. Second, we assessed whether there was a sharing in the TCR repertoire of the intratumoral PD-1^{T} subset with that of the other subsets. Analysis of Eomes and T-bet expression in cells with different levels of PD-1 expression showed that, in contrast to what is observed during chronic LCMV infection18, expression of both transcription factors in human TILs is not correlated with the level of PD-1 (Supplementary Fig. 1i). Furthermore, analysis of T cell receptor (TCR) beta sequences extracted from RNA expression data22 revealed that the PD-1^{T} subset was characterized by a significantly higher clonality, with the top 30 clones contributing close to 90% of the entire TCR repertoire (Fig. 1e). While some sharing of the top 30 clones with PD-1^{N} and PD-1^{-} TILs could be observed, the abundance of these clones was significantly lower in the other two subsets (Fig. 1f, Supplementary Table 1).

The observed clonal expansion of one or a few dominant clones within the PD-1^{T} cell population suggested that the PD-1^{T} phenotype may be driven by TCR triggering (Supplementary Fig. 2a). Consistent with this hypothesis, we observed a high expression of the co-stimulatory receptor CD137 (4-1BB) on cells with high PD-1 levels (Fig. 1g), potentially reflecting recent antigen encounter23. Recent data in melanoma indicate that tumor-reactive T cells are enriched in PD-1^{+} and PD-1 high populations relative to the bulk T cell population13,24–26, although from this work it is unclear whether tumor recognition potential differs between subsets with high and intermediate expression of PD-1. To test whether the PD-1^{T} and PD-1^{N} TIL subsets may differ in their capacity for tumor recognition, we first expanded the PD-1 subsets from eight tumors under the conditions used to generate TIL products for adoptive transfer24 (Supplementary Fig. 2b, note that the PD-1^{T} subset is dysfunctional directly *ex vivo*). During *in vitro* expansion, PD-1 expression on the PD-1^{N} and in particular PD-1^{T} TILs was reduced, and PD-1^{T} TILs regained their capacity to exert effector functions (Fig. 1h). Strikingly, subsequent co-culture of expanded PD-1^{T}, PD-1^{N} and PD-1^{-} TIL populations with autologous tumor digests revealed that, for seven out of eight patients, tumor reactivity was enriched in (n=1) or almost fully restricted to (n=6) the PD-1^{T} TIL derived cell populations. In one patient, tumor recognition was observed in both PD-1^{T} and PD-1^{N} TILs (Fig. 1i and Supplementary Fig. 2b+c).

The transcriptional profile of PD-1^{T} TILs is distinct from both human PD-1^{N} TILs and PD-1^{hi} T cells in chronic viral infection

Having established that PD-1^{T} T cells in human lung cancer are enriched for tumor reactivity but display phenotypic differences to previously described dysfunctional states, we

further characterized this cell population by analysis of RNAseq data from 11 human lung cancers (Supplementary Fig. 1f, sample QC in Supplementary Fig. 1g). Principal component analysis of the gene expression profiles of sorted PD-1^{T}, PD-1^{N} and PD-1^{-} TILs, and peripheral blood CCR7^{-} CD45RA^{-} effector memory (T_{EM}) CD8^{+} T cells from healthy donors, showed that – as expected – all three TIL populations cluster away from peripheral blood T_{EM} cells (Fig. 2a). Strikingly, PD-1^{N} and PD-1^{-} TILs showed almost overlapping gene expression profiles, whereas PD-1^{T} TILs displayed a gene signature that was markedly distinct from both other subsets. Specifically, a total of 577 genes (including *PDCD1* itself, Supplementary Fig. 3a). were significantly upregulated or downregulated (log2 fold change >1, adjusted p-value <0.01) between PD-1^{T} and PD-1^{N} TILs. In contrast, only eight genes showed significantly different expression between PD-1^{N} and PD-1^{-} TILs (Fig. 2b, Supplementary Table 2). Hierarchical clustering analysis revealed eight clusters of genes that displayed distinct expression profiles between PD-1^{T} and PD-1^{N} TILs (Fig. 2c, Supplementary Table 2). Of note, gene expression profiles were highly similar within the PD-1^{T} samples from different patients, in spite of variation in histologic subtype (five adenocarcinomas, four squamous cell carcinomas and two sarcomatoid carcinomas, Supplementary Fig. 3b). We then used pathway-enrichment analysis to identify biological processes that were substantially changed in PD-1^{T} TILs (Fig. 2d). In contrast to exhausted T cells in chronic infection, which lose their proliferative capacity during exhaustion8, genes involved in cell cycle regulation and proliferation were among the most upregulated genes in PD-1^{T} TILs (Fig. 2e). Sorted PD-1^{T} TILs also showed a significantly higher expression of the proliferation marker Ki67 (*MKI67*) at the protein level, which was maintained after 48 hrs of culture without further stimulation (Fig. 2f). Cell cycle analysis revealed a significantly higher percentage of cells in S- and G2/M-phase within the PD-1^{T} subset (PD-1^{T}: 9.1±4.6%; PD-1^{N}: 1.75±1.1%; PD-1^{-}: 0.5±0.4%, PD-1^{T} KI67^{+}: 23.8±8%), confirming that these cells are able to progress through the cell cycle. Further processes that were highly altered in PD-1^{T} TILs related to cell migration and metabolism, indicating that the changes in PD-1^{T} TILs comprise a broad spectrum of core cellular processes.

We observed increased mRNA levels for the inhibitory receptors Tim-3, Lag-3, and CTLA-4, coinciding with their increased protein levels on PD-1^{T} T cells (Fig. 1). PD-1^{T} TILs also showed high expression of a wide array of other receptors with known inhibitory function including CD200, CD109, CD39 (*ENTPD1*), as well as glucocorticoid-induced TNFR-related protein (GITR, *TNFRSF18*), and displayed reduced expression of activating receptors such as CD26 (*DPP4*) at both the RNA and protein level (Fig. 3a,b). In addition, genes encoding receptors with potential inhibitory function that have recently been identified by single cell sequencing of exhausted CD8^{+} TILs in hepatocellular carcinoma27, including *LAYN*, *SNAP47* and *PHLDA1,* were highly expressed by PD-1^{T} T cells (Fig. 3c). High clonal expansion of T cells is generally associated with expression of the senescence marker KLRG128 and loss of the co-stimulatory receptor CD27. However, PD-1^{T} TILs showed lower KLRG1 and higher CD27 expression than their PD-1^{N} and PD-1^{-} counterparts (Fig. 3d).

To further test to what extent PD-1^{T} T cells in human cancer are distinct from the exhausted state that occurs in chronic viral infection, we performed gene set enrichment analysis using established exhaustion signatures from T cells in chronic infection or cancer. Initially, we

compared the exhaustion signature derived from virus-specific exhausted T cells in chronic LCMV infection29 with both PD-1^{T} and PD-1^{N} TILs, demonstrating a similar enrichment of this signature in both subsets (Fig. 3e,f). We also compared human PD-1^{T} and PD-1^{N} TILs with respect to the gene signature that is shared by T cells in early- and late-stage murine tumors30. Also in this case, the gene signature was equally enriched in both PD-1^{T} and PD-1^{N} subsets (Fig. 3e,g). As these gene sets may describe different subsets of exhausted T cells, we also included gene sets from human or murine cancer6,27,31,32, human chronic viral infections33,34 or murine LCMV infection35, that were derived from either PD-1^{hi} subsets or from T cells expressing surface markers that are also upregulated in PD-1^{T} TILs (e.g. Tim-3), and thus might better reflect the latter subset. Comparison of these gene signatures revealed that PD-1^{T} T cells were most similar to exhausted PD-1 bright T cell populations in human cancers that were identified by single cell sequencing (Supplementary Fig. 3c). In contrast, the lowest similarity was observed between PD-1^{T} cells and exhausted Tim-3^{+}PD-1^{+} T cells in murine cancer (Supplementary Fig. 3d). Interestingly, while an intermediate overlap with signatures from PD-1^{hi} T cells in chronic infections was observed, shared genes mostly related to processes involved in cell division and proliferation. In contrast, the enriched genes from exhausted cells in human cancer were associated with T cell activation and immune response (Supplementary Fig. 3e).

PD-1^{T} TILs display profound alterations in metabolism

Recent data from murine tumor models have shown that T cells undergo profound metabolic changes upon entering the TME which lead to metabolic insufficiency36–38. While activated T cells utilize anaerobic glycolysis to meet the increasing demands necessary for proliferation and cytokine production39,40, they also become increasingly dependent on mitochondrial fatty acid oxidation for memory formation41. However, glucose deprivation in the TME and loss of mitochondrial function have been found to impair the antitumor activity of T cells36–38. Thus, we next investigated whether PD-1^{T} TILs display alterations in glucose, lipid and mitochondrial metabolism using metabolic dyes. Strikingly, PD-1^{T} TILs showed a significantly increased glucose uptake (detected by 2-NBDG) compared to both other subsets (Fig. 4a,b). A recent study observed a similar increase in exhausted HBV-specific T cells42. Notably, while T cells need increased glycolytic activity to execute effector functions, prolonged glycolysis has been found to impair antitumor function of CD8^{+} T cells, thereby contributing to their dysfunction43. Similar to the upregulation of glycolysis, lipid uptake (Bodipy 500) and content (Bodipy 493) as well as expression of the scavenger receptor CD36, which mediates uptake of fatty acids, were clearly increased in PD-1^{T} TILs (Fig. 4a+c). In order to benchmark the magnitude of these alterations, we used the changes in circulating T cells upon anti-CD3/anti-CD28 stimulation as a reference, demonstrating that the changes between PD-1^{T} and both other subsets were of a similar magnitude as seen upon peripheral blood T cell activation (Supplementary Fig. 4a). Notably, despite having a slightly larger mitochondrial mass as indicated by mitotracker green (MTG) staining (Fig. 4a,d), PD-1^{T} TILs showed a significantly reduced mitochondrial membrane potential (mitotracker red, MTR) ($\Delta\Psi m$), which was retained even after normalization of $\Delta\Psi m$ to the mitochondrial mass (MTR/MTG ratio), indicating mitochondrial dysfunction (Fig. 4a,d). Transmission electron microscopy confirmed that, while PD-1^{T} TILs show an increase in mitochondria numbers, these mitochondria display profound morphological

changes, with reduced cristae numbers and with a trend towards reduced cristae length (Fig. 4e). PD-1^{T} TILs not only normalized their PD-1 expression and function after *in vitro* expansion but also their metabolism, suggesting that the metabolic dysfunction of this T cell pool can also be reverted outside of the TME (Supplementary Fig. 4b).

PD-1^{T} TILs possess an inherited state of dysfunction

As shown above (Fig. 1h), *in vitro* expansion in the presence of IL-2 can restore cytokine production and reduce PD-1 expression of PD-1^{T} TILs. Nevertheless, expanded PD-1^{T}–derived TILs still expressed higher levels of the inhibitory receptors Tim-3 and Lag-3 compared to the other two subsets (Fig. 5a), potentially suggesting an underlying state of dysfunction. Transcriptome and functional analyses revealed changes in interleukin-10 (IL-10) and pSTAT3 signaling between PD-1^{T} TILs and the PD-1^{N}/PD-1^{-} subsets (Supplementary Fig. 5a,b). In addition, we found IL-10 to be widely expressed by monocytes and tumor cells in NSCLC (but not by PD-1^{T} cells themselves), and the number of IL-10 producing cells correlated with the number of PD-1^{T} TILs (Fig. 5b and Supplementary Fig. 5c). Strikingly, when we exposed IL-2 expanded TIL subsets to IL-10, PD-1^{T}-derived TILs rapidly re-expressed high levels of PD-1, whereas no substantial effect on PD-1^{N}- and PD-1^{-}-derived TIL subsets was observed (Fig. 5c). Similarly, expansion in IL-10 reduced IFN-γ production, with the most severe impairment in PD-1^{T}–derived TILs (Fig. 1h, Fig. 5d). The differential effect of IL-10 on PD-1^{T} TILs was not due to increased IL-10R signaling, as shown by comparable downregulation of IL-10R and increase in perforin expression, a known downstream effect of IL-10R signaling44, in all subsets (Fig. 5e). These findings suggest that PD-1^{T} TILs are particularly susceptible to immunosuppressive factors such as IL-10 due to an inherited state of dysfunction, which may impede efforts to reinvigorate these cells.

PD-1^{T} TILs acquire a novel effector function and predict response to PD-1 blockade

While PD-1^{T} TILs were highly dysfunctional in terms of classical CD8^{+} T cell effector cytokine secretion, transcriptome analysis revealed that the effector chemokine *CXCL13* was among the most upregulated genes within this subset (Supplementary Table 2 and Fig. 3a). PD-1^{T} TILs not only expressed, but also constitutively secreted CXCL13 (Fig. 6a and Supplementary Fig. 6a). CXCL13 exclusively binds to the chemokine receptor CXCR5, which is normally expressed on B cells and CD4^{+} follicular helper T (Tfh) cells, but has recently been shown to also mark a subset of exhausted virus-specific CD8^{+} T cells in lymphoid tissues that responds to PD-1 blockade45,46. The main function of CXCL13 is to control the recruitment and organization of B cells within lymphoid follicles47. Thus, CXCL13 secretion by PD-1^{T} TILs might serve to attract other immune cell subsets to the TME. To address this, we investigated the ability of sorted peripheral blood CXCR5^{+} immune cell subsets including CD8^{+}, CD4^{+} T cells and B cells from NSCLC patients to migrate in response to CXCL13 *in vitro* (Fig. 6b). We found that all subsets showed chemotaxis to CXCL13 compared to CXCR5^{-} CD3^{+} T cells, with migration of CXCR5^{+} CD4^{+} T cells being the most pronounced. We hypothesized that if PD-1^{T} TILs mediate recruitment of Tfh and B cells, these three subsets would co-localize within the TME. We therefore identified PD-1^{T} TILs in NSCLC samples by CD8/PD-1 double staining and digital image analysis using an algorithm to detect CD8^{+} TILs with strong PD-1 expression

(Fig. 6c-e, see also below). Strikingly, PD-1^{T} TILs were predominantly localized in intra- and peritumoral tertiary lymphoid structures (TLS) in close vicinity to Tfh, marked by CD4 and Bcl6, and B cell infiltrates (Fig. 6d,f). In most tumors, PD-1^{T} TILs surrounded the central B cell area and were found at the tumor-host interface (Fig. 6e), suggesting that PD-1^{T} TILs may play an active role in the recruitment of immune subsets to the TME.

Based on the observation that PD-1^{T} TILs are the most prominent tumor-reactive T cell pool in NSCLC (Fig. 1i), we investigated whether these cells might also be predictive for response to PD-1-targeting therapies. To this end, we used parallel analysis of two parts of a set of tumor samples to establish an algorithm-based quantitative PD-1 immunohistochemistry (IHC) assay for paraffin-embedded tissue by comparing with flow cytometric PD-1^{T} quantification of the same sample. The algorithm generated in this manner was subsequently validated by independent analysis of a second and third set of slides from the same tumor samples at two different institutes (see Methods section, Supplementary Fig. 6b,c). Having validated this strategy for quantitative analysis of PD-1^{T} cell levels, we applied this method to evaluate the presence of PD-1^{T} cells in pretreatment biopsies of 21 stage IV NSCLC patients undergoing anti-PD-1 therapy (Supplementary Fig. 6d). Strikingly, presence of PD-1^{T} TILs very strongly predicted response to therapy (Fig. 6g), and also correlated with increased overall survival (HR 0.16 (95% CI 0.05-0.52), $p<0.05$) and durable responses (Fig. 6h,i) in this cohort. In contrast, the predictive value of PD-1^{N} TILs was lower (Supplementary Fig. 6e). These findings indicate that the presence of PD-1^{T} TILs may represent a novel biomarker for response to agents that target the PD-1/PD-L1 axis.

Discussion

Cancer immunotherapies that reactivate tumor-specific T cells through blockade of the PD-1/PD-L1 axis have emerged as a promising treatment option for many cancers48. However, prior studies indicate that not all PD-1^{+} cells might respond equally to anti-PD-1 treatment14,17. Here we describe the properties of T cells with different PD-1 expression levels in NSCLC and their potential relationship with immune-mediated tumor control. Our data show that PD-1^{T} TILs in NSCLC are a highly exhausted T cell subset that displays profound molecular, metabolic and functional differences relative to PD-1^{N} and PD-1^{-} TILs, and that also contains the bulk of the tumor recognition potential of intratumoral CD8^{+} lymphocytes.

T cell exhaustion was originally described in murine chronic viral infections, where persistent antigenic stimulation may be the main driver of this dysfunctional state8. In cancer, the TME is likely to provide additional immunosuppressive stimuli that may further modulate exhaustion. Supporting this hypothesis, we found that, while PD-1^{T} TILs share key characteristics such as overexpression of inhibitory receptors and loss of effector cytokine secretion with PD-1^{hi} T cells from chronic infection, they clearly differ in many cellular core processes. First, the clear relationship between Eomes and T-bet expression with high and intermediate PD-1 expression levels in chronic infections18 is not present in the PD-1 subsets in human lung cancer. Second, PD-1^{T} TILs are a highly clonal T cell population with a predominance of TCRs that are present at low abundance in PD-1^{N} TILs, suggesting an antigen-driven expansion of this subset rather than a gradual progression in

exhaustion from PD-1^{N} to PD-1^{T} TILs as observed in chronic LCMV infection18. Third, in contrast to the loss of proliferation in exhausted T cells in chronic infection, processes involved in cell cycle and cell division were highly upregulated in lung cancer-derived PD-1^{T} TILs, potentially reflecting clonal expansion of this subset upon *in vivo* antigen stimulation. Fourth, PD-1^{T} TILs in human lung cancer show profound metabolic alterations, with increased glycolysis and defects in mitochondrial metabolism. Competition for glucose in the TME due to increased glycolysis of tumor cells has been shown to impair T cell functionality in murine tumor models37. Thus, the limitation of metabolic intermediates that are necessary for antitumor activity, might further augment dysfunction of PD-1^{T} TILs. Fifth, the gene signature of exhausted T cells from chronic viral infections is not enriched in PD-1^{T} TILs relative to PD-1^{N} TILs, and the same applies to the exhaustion signature of early and late-stage tumors from murine cancer models30, the exhaustion signatures seen in T cells from human infections33,34, or the signature of PD-1^{hi} T cells in LCMV infection35. Together, these observations provide compelling evidence that PD-1^{T} TILs in human lung cancer display a state of dysfunction that is distinct to those states that have been previously described.

A striking aspect of this cell state is the constitutive secretion of the chemoattractant CXCL13. Three recent studies investigating T cells in human melanoma and hepatocellular carcinoma identified *CXCL13* as one of the significantly upregulated genes in highly exhausted TILs6,27,31, and the current data, as well as data from a recent study in breast cancer49, show that this mRNA expression is accompanied by constitutive protein secretion. Furthermore, we observed that CXCL13 secreting PD-1^{T} TILs were predominantly present in TLS, suggesting a possible involvement of these cells in the formation of TLS.

The observation that tumor reactivity is to a very large extent restricted to the PD-1^{T} TIL subset makes quantification of this subset an attractive proxy for the anti-tumor potential of the intratumoral T cell pool. In support of this, retrospective analysis of PD-1^{T} TIL infiltration in pretreatment biopsies of NSCLC patients undergoing anti-PD-1 therapy revealed a clear correlation between the frequency of these cells and both treatment response and patient survival. This clear relationship may either reflect the direct tumoricidal capacity of these cells following PD-1 blockade, or their ability to recruit other immune cells that mediate the anti-tumor immune response. Collectively, our findings describe PD-1^{T} TILs in human lung cancer as a highly distinct cellular pool that has not only lost classical CD8^{+} effector functions but has developed a novel functionality and holds the potential to predict patient outcome upon PD-1 targeting therapies. Future work should address whether the targeting of any of the other of the large number of known or potential inhibitory receptors on these cells can further increase their activity, an effort that is of particular interest in view of the high intrinsic tumor reactivity of this subset. In parallel, it will be of interest to establish how PD-1^{T} TIL are influenced by PD-1 blockade in human cancer samples, and to validate PD-1^{T} TILs as a predictive marker for response to cancer immunotherapy in larger prospective trials.

Online Methods

Patient characteristics and tumor sample processing

Fresh tumor samples were collected from individuals with non-small cell lung cancer undergoing primary surgical treatment between January 2013 and June 2016 at the University Hospital Basel, Switzerland and at the Ortenau Klinikum, Germany. Paraffin-embedded tumor biopsies were collected from stage IV non-small cell lung cancer patients undergoing treatment with nivolumab between April 2015 and June 2017 at the University Hospital Basel and the Cantonal Hospital Baselland, Switzerland. Detailed patient characteristics are provided in Supplementary Table 3 and 4. The study was approved by the local Ethical Review Board (Ethikkommission Nordwestschweiz), performed in compliance with all relevant ethical regulations, and all patients consented in writing to the analysis of their tumor samples.

Resected solid tumor lesions were immediately processed into single cell suspensions by mechanical dissociation and enzymatic digestion using accutase (PAA), collagenase IV (Worthington), hyaluronidase (Sigma) and DNAse type IV (Sigma). All samples were cryopreserved until further usage.

Antibodies and phenotypic characterization of T cells

Anti-CD19 APC-eFluor780 (SJ25C1), -CD45 PerCP-Cy5.5 (2D1), -CD56 PE (CMSSB), -CD3 APC-eFluor780 (SK7), -Lag-3 FITC (3DS223H), -TIGIT PE (MBSA43), -2B4 FITC (eBioDM244), -CD137 FITC (4B4), -IL-2 PE (MQ1-17H12), -TNF-α APC (MAb11), -CD26 FITC (2A6), -CXCR5 Biotin (MU5UBEE), -ICOS FITC (ISA-3), -CD38 APC (HIT2), -Eomes eFluor660 (WD1928), -T-bet PE (eBio4B10), -pSTAT3 PE (LUVNKLA) were purchased from eBioscience. Anti-CD4 BV711 (SK3), -PD-1 PE-Cy7 (EH12.1), -PD-1 AlexaFluor647 (EH12.1), -BTLA PE (J168-540), -IFN-γ BV421 (4S.B3), -CD27 BV711 (M-T271), -CD28 PE-Cy7 (CD28.2), -Ki67 BV421 (B56), -CD20 BV711 (2H7), and Streptavidin BV711 and Streptavidin BV605 were purchased from BD. Anti-CD8 BV605 (RPA-T8), -CD8 BV711 (SK1), -CD8 PE-Cy7 (SK1), -CD4 PE (SK3), -CD11b PE (ICRF44), -CD11c PE (3.9), -CD14 PerCP-Cy5.5 (HCD14), -CD45 APC-eFluor780 (HI30), -Tim-3 BV421 (F38-2E2), -IL10 PE (JES3-9D7), -CD200 BV421 (OX-104), -CD109 PE (W7C5), -GITR APC (621), -CD39 FITC (A1), -CD127 BV605 (A019D5), -CCR7 PE (G043H7), -CD45RA BV421 (HI100), -CD62L BV421 (DREG-56), -KLRG1 BV421 (2F1/KLRG1), -CD36 APC (5-271), -CCR6 PE-Cy7 (G034E3), -CCR4 PE-Cy7 (TG6/CCR4), -CXCR3 PE (G025H7), -HLA ABC APC-Cy7 (W6/32), and Streptavidin PE-Cy7 were purchased from Biolegend and anti-CXCL13 APC (53610) from R&D Systems.

For phenotypic characterization of cryopreserved tumor digests, samples were thawed, washed, resuspended in 50 µl PBS and blocked with Fc receptor blocking agent (eBioscience) for 20 min at 4°C. Cells were stained with live/dead Zombie UV (Invitrogen). Cells were washed, resuspended in 50 µl of staining buffer (PBS, 2mM EDTA, 0.1% NaN_3, 2% fetal calf serum) containing antibodies for surface staining and incubated for 20min at 4°C. Corresponding isotype antibodies were used as a control. After washing twice, secondary antibodies were added where indicated for 20 min at 4°C. After washing, cells

were taken up in 200 µl Fixation Buffer (eBioscience). For intracellular staining, cells were washed twice, fixed and permeabilized using Fix/Perm solution (eBioscience) for 30 min at room temperature. After washing twice, cells were resuspended in 1x Permeabilization Buffer (eBioscience) containing antibodies for 40 min at room temperature. All samples washed twice before acquisition.

For analysis of pSTAT3 levels, digests were thawed and cultured overnight. The next day, digests were incubated for 15 min at 37°C in the presence or absence of 20 IU IL-10 (Peprotech). After washing, cells were fixed with 100 µl Fixation buffer (eBioscience) for 15 min at 37°C. After washing, cells were resuspended while vortexing by dropwise addition of -20°C pre-chilled True-Phos™ Perm buffer (Biolegend) and incubated for 1 hr at -20°C. After washing, antibody staining was performed as described above.

Acquisition of samples was carried out on a BD LSR Fortessa Cell analyzer (BD Bioscience). Data were collected using the BD FACS Diva Software version 7 and further analyzed with FlowJo v10.0.6 (Tree Star Inc.), and GraphPad Prism v6.0e (GraphPad Software Inc.). Data were gated on live cells (Zombie UV negative) and single cells. The gating strategy for PD-1 subsets is shown in detail in Fig. 1.

T cell sorting and *in vitro* expansion of CD8$^+$ T cells

For isolation of indicated cell subsets, cells were thawed, washed and resuspended in 300 µl staining buffer containing antibodies. After 20 min incubation at 4°C, cells were washed twice and cell sorting was performed using a BD FACS Aria III. Cells were gated on live (PI negative), single cells, CD45$^+$, CD3$^+$, bulk (CD14, CD19, CD56, CD4) negative and CD8$^+$ cells, and on the population of interest. The detailed gating strategy used to sort intratumoral lymphocyte subsets based on PD-1 expression is shown in Supplementary Fig. 3. App. 3x10^4 cells were directly sorted in lysis buffer (Arcturus Pico Pure RNA Isolation Kit) and used for RNA sequencing. The remainder of the cells were cultured *in vitro* for further experiments.

From eight tumor samples, 5 x 10^3 T cells PD-1^T, PD-1^N, and PD-1$^-$ T cells were expanded *in vitro* using an excess of irradiated allogeneic feeder cells (4,000 rad) pooled from three donors in T cell medium (1:1 mix of AIMV medium (Thermo Fisher) and RPMI 1640 medium (Sigma), 5% human serum (mix of 3 donors, Blutspendezentrum Basel), 100 units penicillin (Sigma), 100 µg/ml streptomycin (Sigma), 2 mM L-glutamine (Sigma), 25 mM HEPES (Sigma)) supplemented with 3,000 IU of IL-2 (Peprotech) and 30 ng/ml anti-CD3 (OKT3, Biolegend)24. Where indicated, cells were expanded with the same protocol containing 100 IU IL-2 and 200 IU IL-10 (Peprotech). After day 5, half of the medium was replaced with fresh medium containing IL-2 every two to three days. Cells were split 1:2 at day 7 or when necessary. At day 15, T cells were tested for PD-1 expression and IFN-γ release or cryopreserved until further analysis. Phenotype and effector functions were consistent between replicate expansions of the same subsets.

Polyclonal stimulation and assessment of target cell recognition

Cryopreserved tumor digests were thawed, washed and cultured at 3 x 10^5 cells in 96-well plates in tumor medium (DMEM (Sigma), 10% fetal bovine serum (Pan Biotech), 1 mM

sodium pyruvate (Sigma), 1x MEM non-essential AA (Sigma), 2 mM L-glutamine, 100 ng/ml penicillin/streptomycin, 50 nM 2-mercaptoethanol (Sigma), 1 mg/ml ciproxin (Bayer)). Cells were stimulated with a suboptimal concentration of 0.5 μg/ml plate bound anti-CD3 (OKT3) and 2 μg/ml soluble anti-CD28 (28.2, eBioscience) for 24 or 48 hrs, as potent co-stimulatory signals may mask some functional defects of T cells14,50. 20 ng/ml IL-10 was added where indicated. Following incubation, supernatants were collected for cytokine/chemokine analysis as indicated. Secretion of indicated cytokines and chemokines was detected using the LEGENDplex™ Human Th Cytokine and Human Proinflammatory Chemokine Panels (Biolegend) as well as the ProcartaPlex Simplex Kits (Invitrogen). For intracellular cytokine staining 1x monensin (eBioscience) was added for the last 5 hrs of culture and cells were analyzed by flow cytometry.

Sorted PD-1 subsets were rested overnight in complete medium (RPMI, 10% human serum, 1 mM sodium pyruvate, 1x MEM non-essential AA, 2 mM L-glutamine, 100 ng/ml penicillin/streptomycin, 1 mg/ml ciproxin). $3x10^4$ cells were stimulated with anti-CD3/anti-CD28 for 48 hrs as described above, and supernatants were collected for cytokine/chemokine analysis.

For investigation of tumor reactivity cryopreserved expanded PD-1 subsets were thawed, washed and rested for 24 hrs in 50 IU IL-2. Cells were washed to remove cytokines and fluorescently labeled with 1 μM carboxyfluorescein succinimidyl ester (CFSE, Life Technologies). Autologous tumor digests were thawed, washed and resuspended in complete medium. Percentage of tumor cells in the digests was previously estimated by flow cytometry by gating on CD45 negative, FSc high cells. 1 x 10^5 CFSE-labeled T cells were co-cultured with autologous digest at an effector : target cell ratio of 1 : 1. A condition with anti-HLA class I blocking antibody (w6/32, Invivo Gen) was included to determine HLA class I restriction of the observed reactivity. T cells cultured alone or stimulated with plate bound anti-CD3/anti-CD28 or 50 ng/ml PMA/ 1 μg/ml ionomycin (BD) were used as further controls. After one hour, 1x monensin and 1x brefeldin A (eBioscience) were added for intracellular cytokine staining and cells were incubated overnight before analysis of IFN-γ production by flow cytometry.

Immunometabolism

As no difference in metabolism between fresh and frozen T cells was observed, frozen samples were used for all these experiments. Cryopreserved tumor digests were thawed, washed and rested overnight in tumor medium. The next day, cells were washed and incubated at 2 x 10^5 cells in pre-warmed complete medium containing either 20 μM 2-NBDG (Thermo Fisher), 100 nM Mitotracker Green FM (Thermo Fisher), 100 nM Mitotracker Red CMXRos (Thermo Fisher) or 1 μM Bodipy 500 (Thermo Fisher) for 20 min at 37°C in 96-well round bottom plates. Cells were washed and stained with antibodies against cell surface antigens as described above. For analysis of lipid content 1 μg/ml Bodipy 493 (Thermo Fisher) was added in 1x Permeabilization Buffer for 1 hr at 4°C. Cells were analyzed on a BD LSR Fortessa Cell analyzer and metabolic parameters were quantified as mean fluorescence intensity. Unstained and single stained cells were used as controls.

Electron microscopy

Sorted cells were fixed with 2.5% glutaraldehyde diluted in 0.1M of phosphate buffer solution (PB buffer, Sigma) for 1 hour at room temperature. Cells were spun down and the second fixation step was performed for 1 hour at RT with osmium tetroxide (1%), glutaraldehyde (2.5%) and potassium ferrocyanide 1.5% diluted in 0.1M PB buffer. Cells were washed four times with water and followed by dehydration steps with acetone: 30%-10min, 70%-10min, and 100% 3x10min. Subsequently, the pellet was incubated in Epon resin (100%) overnight at RT and then polymerized in resin at 60°C for 2 days. 50nm thin sections were stained with 4% uranyl acetate, followed by Reynolds lead citrate. Images were taken at 80kV with a CM100 and TVIPS F416 camera. Cells were randomly chosen on the section and 6 images at 4800x magnification + 15 images at 11000x magnification were taken.

Chemotaxis

Chemotaxis assays were carried out as described previously45,51, using 96-well transwell plates with 5 μm pores (Corning). $CXCR5^+$ $CD8^+$, $CD4^+$ T cells and $CD19^+$ B lymphocytes as well as $CXCR5^-$ $CD3^+$ T cells were sorted from patient PBMCs and rested overnight in complete medium. 2.5 x 10^4 cells were seeded onto upper wells in 100 μl medium. The bottom wells contained 235 μl PBS with or without 1 μg/ml recombinant human CXCL13 (R&D). After 3 hrs, 50 μl Precision Count Beads™ (Biolegend) were added and transmigrated cells were counted by flow cytometry. Cell numbers were calculated using the following formula: *absolute cell count = cell count / bead count x total bead concentration*. The chemotactic index was calculated as the ratio of transmigrated $CXCR5^+$ cells over transmigrated $CXCR5^-$ control T cells.

RNA sequencing, molecular signatures and TCR analysis

High molecular weight RNA (> 200 bp) was extracted from 2,000–40,000 cells collected in XB buffer (Life Technologies) using the Arcturus Pico Pure RNA Isolation Kit (Life Technologies). Residual genomic DNA was removed using the RNase free DNase set (Qiagen). RNA quality and quantity were determined by capillary electrophoresis on Eukaryote Total RNA pico chips (Agilent Technologies). High quality RNA (RIN> 7) was obtained for all samples.

To prepare and amplify cDNA from 500 pg of total RNA, the SMART-Seq v4 Ultra Low Input RNA Kit (Clontech) was used according to manufacturer's instructions. Amplified cDNA was quality controlled by capillary electrophoresis on a Bioanalyzer using High Sensitivity chips (Agilent Technologies). Then, 150 pg of amplified cDNA was used for Nextera XT library preparation (Illumina) according to manufacturer's instructions. Sequencing libraries were quantified with the Kapa Library Quantification kit (Kapa Biosystems) and quality control was performed by capillary electrophoresis on a Bioanalyzer using High Sensitivity chips (Agilent Technologies). Libraries were sequenced on a HiSeq4000 sequencer (Illumina) for 2 x 50 cycles using HiSeq 3000/4000 PE cluster generation kits and HiSeq 3000/4000 SBS Kit sequencing reagents (Illumina).

All samples were processed as follows: First, reads were mapped against the human genome (hg19) using GSNAP [ID: 27008021]. Second, mapped reads were assigned to human genes based on GRCh37.75 annotation. Gene expression levels were computed as Reads Per Kilobase of transcript per Million mapped reads (RPKM) values as described by Mortazavi et al.52 using in-house tools. The LME model framework was used to assess differential expression for each gene using log2 RPKM values. The individual donor was treated as a random effect and the three PD-1 subgroups were used as fixed effects. Significantly regulated genes were reported at Benjamini–Hochberg [https://www.jstor.org/stable/2346101] FDR<0.01 and an absolute log2 fold-change ≥1. In total, 997 annotated genes were detected. Principal component analysis was performed on mean centered data using in-house R scripts. Hierarchical clustering was performed on the set of significantly regulated genes using complete-linkage and Euclidean distance. Sub-clusters were derived using the R function cutree53. The Hypergeometric test was conducted to identify enriched biological processes annotated by gene ontology (GO) terms for each sub-cluster using the 'GOHyperGParams' method from the R package GOstats [ID: 17098774]. P-values were corrected using Benjamini-Hochberg method. All biological processes with the adjusted P value less than 0.05 were considered as significantly enriched. Gene set enrichment analysis (GSEA, http://broadinstitute.org/gsea) was used to determine whether predefined exhaustion gene sets showed enrichment in the PD-1^{T} and PD-1^{N} subsets (Crawford et al., 2014; Schietinger et al., 2016, Gupta et al., 2015, Quigley et al., 2010, Zheng et al., 2017, Doering et al., 2012, Baitsch et al., 2011, Tirosh et al., 2016, Singer et al., 2016). T cell receptor beta chain clonality was assessed using the MiXCR tool using standard parameters of the RNAseq workflow. TCR clonality was analyzed using the R package tcR [ID: 26017500]54. RNA sequencing data are available at NCBI GEO: (GSE99531).

Immunohistochemistry and digital image analysis

Strict serial sections 4 μm were cut from formalin-fixed paraffin embedded tissue blocks of primary NSCLC. Deparaffinization was performed according to standard protocols. Sections were pre-treated and stained with monoclonal antibodies directed against CD4 (4B12, Novocastra), CD19 (LE-CD19, Dako), CD21 (1F8, Dako), Bcl-6 (PG-B6p, Dako) on a Leica-Bond™ III/max autostainer platform (Leica Biosystems). Stains were detected using anti-Ig coupled horseradish peroxidase with 3,3'-diaminobenzidine (DAB) as substrate. Nuclear counterstaining was performed with Mayer hematoxylin. Immunohistochemical single staining for PD-1 was carried out using a Roche Benchmark Ultra (NAT105, Roche Diagnostics, Ventana/DAB detection). Immunohistochemical double stains for CD8 and PD-1 were performed using the PD-1 staining protocol on a Roche Benchmark Ultra followed by CD8 staining (4B11, Refine Red detection) on a Leica-Bond™ III/max autostainer.

Slides were scanned at high resolution on a CD-IVD certified Philips Ultra Fast Scanner 300 (Philips Digital Pathology Solutions) and digital image analysis was carried out by an experienced pathologist (VHK) using the HALO™ image analysis software, v.2.0.1145.19 (Indica Labs). Classification of PD-1^{T}, PD-1^{N} and PD-1^{-} cells on single stains was performed using computationally derived cutoffs, which were identified by comparing FFPE samples with flow cytometry guided annotation of the PD-1 subsets in matched samples. For

assessment of double stains, marker recognition and color deconvolution was tested and optimized on CD8/PD-1 double positive cells. For TLS assessment, digital slides were reviewed and tertiary lymphoid structures (TLS) were manually annotated.

Statistical analysis

Data are reported as the mean ± SD or mean ± SEM, as specified. Statistical significance was determined using one-way or two-way ANOVA or Mann-Whitney test as indicated (Prism version 7, GraphPad Software). Differences were considered statistically significant if *p<0.05, **p<0.01, ***p<0.001, ****p<0.0001. Only significant p-values are displayed. Unless otherwise specified, experiments were performed without duplicate due to material restrictions. Functional data are representative of at least three experiments.

Supplementary Material

Refer to Web version on PubMed Central for supplementary material.

Acknowledgements

We thank D. Labes and E. Traunecker for exemplary technical assistance with cell sorting, F. Franco and T. Chao for performing electron microscopy analysis, L. Tietze for contribution of tumor samples, B. Dolder-Schlienger for technical assistance, and F. Uhlenbrock and D. Pinschewer for helpful discussions and critical reading of the manuscript. This work was supported by grants from the Swiss National Science Foundation (P300PB_164755/1 to D.S.T., 320030_162575 to A.Z. and 31003A_163204 to P.C.H.), the Research Funds University of Basel (D.S.T.), the Lichtenstein-Stiftung (D.S.T.), the FAG-Basel (D.S.T.), the Dutch Cancer Society Queen Wilhelmina Award NKI 2013-6122 (T.N.S.) and ERC grant SENSIT (T.N.S.).

References

1. Castle JC, et al. Exploiting the mutanome for tumor vaccination. Cancer Res. 2012; 72:1081–1091. [PubMed: 22237626]
2. Heemskerk B, Kvistborg P, Schumacher TN. The cancer antigenome. The EMBO journal. 2013; 32:194–203. [PubMed: 23258224]
3. Mellman I, Coukos G, Dranoff G. Cancer immunotherapy comes of age. Nature. 2011; 480:480–489. [PubMed: 22193102]
4. Schreiber RD, Old LJ, Smyth MJ. Cancer immunoediting: integrating immunity's roles in cancer suppression and promotion. Science. 2011; 331:1565–1570. [PubMed: 21436444]
5. Schietinger A, Greenberg PD. Tolerance and exhaustion: defining mechanisms of T cell dysfunction. Trends in immunology. 2014; 35:51–60. [PubMed: 24210163]
6. Baitsch L, et al. Exhaustion of tumor-specific CD8(+) T cells in metastases from melanoma patients. J Clin Invest. 2011; 121:2350–2360. [PubMed: 21555851]
7. Zajac AJ, et al. Viral immune evasion due to persistence of activated T cells without effector function. The Journal of experimental medicine. 1998; 188:2205–2213. [PubMed: 9858507]
8. Wherry EJ. T cell exhaustion. Nat Immunol. 2011; 12:492–499. [PubMed: 21739672]
9. Wherry EJ, et al. Molecular signature of CD8+ T cell exhaustion during chronic viral infection. Immunity. 2007; 27:670–684. [PubMed: 17950003]
10. Day CL, et al. PD-1 expression on HIV-specific T cells is associated with T-cell exhaustion and disease progression. Nature. 2006; 443:350–354. [PubMed: 16921384]
11. Trautmann L, et al. Upregulation of PD-1 expression on HIV-specific CD8+ T cells leads to reversible immune dysfunction. Nature medicine. 2006; 12:1198–1202.
12. Golden-Mason L, et al. Upregulation of PD-1 expression on circulating and intrahepatic hepatitis C virus-specific CD8+ T cells associated with reversible immune dysfunction. Journal of virology. 2007; 81:9249–9258. [PubMed: 17567698]

13. Ahmadzadeh M, et al. Tumor antigen-specific CD8 T cells infiltrating the tumor express high levels of PD-1 and are functionally impaired. Blood. 2009; 114:1537–1544. [PubMed: 19423728]
14. Thommen DS, et al. Progression of Lung Cancer Is Associated with Increased Dysfunction of T Cells Defined by Coexpression of Multiple Inhibitory Receptors. Cancer immunology research. 2015; 3:1344–1355. [PubMed: 26253731]
15. Schreiner J, et al. Expression of inhibitory receptors on intratumoral T cells modulates the activity of a T cell-bispecific antibody targeting folate receptor. Oncoimmunology. 2016; 5:e1062969. [PubMed: 27057429]
16. Zippelius A, et al. Effector function of human tumor-specific CD8 T cells in melanoma lesions: a state of local functional tolerance. Cancer Res. 2004; 64:2865–2873. [PubMed: 15087405]
17. Blackburn SD, Shin H, Freeman GJ, Wherry EJ. Selective expansion of a subset of exhausted CD8 T cells by alphaPD-L1 blockade. Proc Natl Acad Sci U S A. 2008; 105:15016–15021. [PubMed: 18809920]
18. Paley MA, et al. Progenitor and terminal subsets of CD8+ T cells cooperate to contain chronic viral infection. Science. 2012; 338:1220–1225. [PubMed: 23197535]
19. Grosso JF, et al. Functionally distinct LAG-3 and PD-1 subsets on activated and chronically stimulated CD8 T cells. Journal of immunology. 2009; 182:6659–6669.
20. Sakuishi K, et al. Targeting Tim-3 and PD-1 pathways to reverse T cell exhaustion and restore anti-tumor immunity. The Journal of experimental medicine. 2010; 207:2187–2194. [PubMed: 20819927]
21. Kansy BA, et al. PD-1 Status in CD8(+) T Cells Associates with Survival and Anti-PD-1 Therapeutic Outcomes in Head and Neck Cancer. Cancer Res. 2017; 77:6353–6364. [PubMed: 28904066]
22. Bolotin DA, et al. MiXCR: software for comprehensive adaptive immunity profiling. Nature methods. 2015; 12:380–381. [PubMed: 25924071]
23. Wolfl M, et al. Activation-induced expression of CD137 permits detection, isolation, and expansion of the full repertoire of CD8+ T cells responding to antigen without requiring knowledge of epitope specificities. Blood. 2007; 110:201–210. [PubMed: 17371945]
24. Gros A, et al. PD-1 identifies the patient-specific CD8(+) tumor-reactive repertoire infiltrating human tumors. J Clin Invest. 2014; 124:2246–2259. [PubMed: 24667641]
25. Gros A, et al. Prospective identification of neoantigen-specific lymphocytes in the peripheral blood of melanoma patients. Nature medicine. 2016; 22:433–438.
26. Inozume T, et al. Selection of CD8+PD-1+ lymphocytes in fresh human melanomas enriches for tumor-reactive T cells. Journal of immunotherapy. 2010; 33:956–964. [PubMed: 20948441]
27. Zheng C, et al. Landscape of Infiltrating T Cells in Liver Cancer Revealed by Single-Cell Sequencing. Cell. 2017; 169:1342–1356 e1316. [PubMed: 28622514]
28. Henson SM, et al. KLRG1 signaling induces defective Akt (ser473) phosphorylation and proliferative dysfunction of highly differentiated CD8+ T cells. Blood. 2009; 113:6619–6628. [PubMed: 19406987]
29. Crawford A, et al. Molecular and transcriptional basis of CD4(+) T cell dysfunction during chronic infection. Immunity. 2014; 40:289–302. [PubMed: 24530057]
30. Schietinger A, et al. Tumor-Specific T Cell Dysfunction Is a Dynamic Antigen-Driven Differentiation Program Initiated Early during Tumorigenesis. Immunity. 2016; 45:389–401. [PubMed: 27521269]
31. Tirosh I, et al. Dissecting the multicellular ecosystem of metastatic melanoma by single-cell RNA-seq. Science. 2016; 352:189–196. [PubMed: 27124452]
32. Singer M, et al. A Distinct Gene Module for Dysfunction Uncoupled from Activation in Tumor-Infiltrating T Cells. Cell. 2016; 166:1500–1511 e1509. [PubMed: 27610572]
33. Gupta PK, et al. CD39 Expression Identifies Terminally Exhausted CD8+ T Cells. PLoS pathogens. 2015; 11:e1005177. [PubMed: 26485519]
34. Quigley M, et al. Transcriptional analysis of HIV-specific CD8+ T cells shows that PD-1 inhibits T cell function by upregulating BATF. Nature medicine. 2010; 16:1147–1151.

35. Doering TA, et al. Network analysis reveals centrally connected genes and pathways involved in CD8+ T cell exhaustion versus memory. Immunity. 2012; 37:1130–1144. [PubMed: 23159438]
36. Scharping NE, et al. The Tumor Microenvironment Represses T Cell Mitochondrial Biogenesis to Drive Intratumoral T Cell Metabolic Insufficiency and Dysfunction. Immunity. 2016; 45:701–703. [PubMed: 27653602]
37. Chang CH, et al. Metabolic Competition in the Tumor Microenvironment Is a Driver of Cancer Progression. Cell. 2015; 162:1229–1241. [PubMed: 26321679]
38. Ho PC, et al. Phosphoenolpyruvate Is a Metabolic Checkpoint of Anti-tumor T Cell Responses. Cell. 2015; 162:1217–1228. [PubMed: 26321681]
39. Sena LA, et al. Mitochondria are required for antigen-specific T cell activation through reactive oxygen species signaling. Immunity. 2013; 38:225–236. [PubMed: 23415911]
40. MacIver NJ, Michalek RD, Rathmell JC. Metabolic regulation of T lymphocytes. Annu Rev Immunol. 2013; 31:259–283. [PubMed: 23298210]
41. van der Windt GJ, et al. CD8 memory T cells have a bioenergetic advantage that underlies their rapid recall ability. Proc Natl Acad Sci U S A. 2013; 110:14336–14341. [PubMed: 23940348]
42. Schurich A, et al. Distinct Metabolic Requirements of Exhausted and Functional Virus-Specific CD8 T Cells in the Same Host. Cell reports. 2016; 16:1243–1252. [PubMed: 27452473]
43. Sukumar M, et al. Inhibiting glycolytic metabolism enhances CD8+ T cell memory and antitumor function. J Clin Invest. 2013; 123:4479–4488. [PubMed: 24091329]
44. Wang Y, et al. Autocrine Complement Inhibits IL10-Dependent T-cell-Mediated Antitumor Immunity to Promote Tumor Progression. Cancer discovery. 2016; 6:1022–1035. [PubMed: 27297552]
45. Im SJ, et al. Defining CD8+ T cells that provide the proliferative burst after PD-1 therapy. Nature. 2016; 537:417–421. [PubMed: 27501248]
46. He R, et al. Follicular CXCR5-expressing CD8+ T cells curtail chronic viral infection. Nature. 2016; 537:412–428. [PubMed: 27501245]
47. Ansel KM, et al. A chemokine-driven positive feedback loop organizes lymphoid follicles. Nature. 2000; 406:309–314. [PubMed: 10917533]
48. Zou W, Wolchok JD, Chen L. PD-L1 (B7-H1) and PD-1 pathway blockade for cancer therapy: Mechanisms, response biomarkers, and combinations. Science translational medicine. 2016; 8:328rv324.
49. Gu-Trantien C, et al. CXCL13-producing TFH cells link immune suppression and adaptive memory in human breast cancer. JCI Insight. 2017; 2
50. Gunnlaugsdottir B, Maggadottir SM, Ludviksson BR. Anti-CD28-induced co-stimulation and TCR avidity regulates the differential effect of TGF-beta1 on CD4+ and CD8+ naive human T-cells. International immunology. 2005; 17:35–44. [PubMed: 15557315]
51. Allen CD, et al. Germinal center dark and light zone organization is mediated by CXCR4 and CXCR5. Nat Immunol. 2004; 5:943–952. [PubMed: 15300245]
52. Mortazavi A, Williams BA, McCue K, Schaeffer L, Wold B. Mapping and quantifying mammalian transcriptomes by RNA-Seq. Nature methods. 2008; 5:621–628. [PubMed: 18516045]
53. Becker RA, Chambers JM, WIlks AR. The New S Languate. Wadsworth & Brooks/Cole; Monterey: 1988.
54. Nazarov VI, et al. tcR: an R package for T cell receptor repertoire advanced data analysis. BMC Bioinformatics. 2015; 16:175. [PubMed: 26017500]

Europe PMC Funders Author Manuscripts

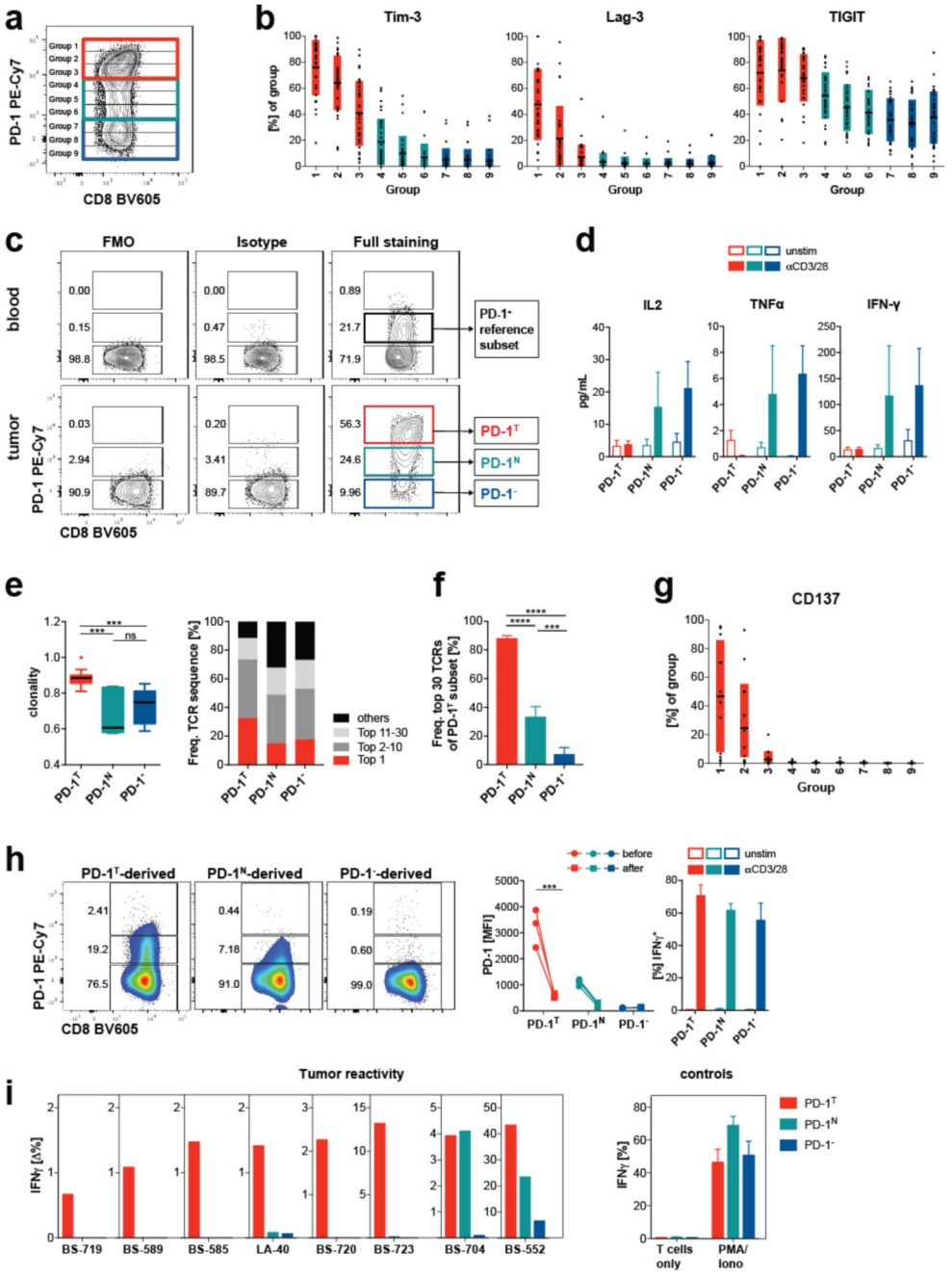

Figure 1. Co-receptor expression, functionality and tumor reactivity of CD8$^+$ PD-1$^+$ TIL populations in NSCLC.

(**a**) Gating strategy of CD8$^+$ TIL subsets according to PD-1 MFI for subgroup analysis, one exemplary NSCLC specimen is depicted. (**b**) Co-expression of other immune checkpoints on PD-1 subgroups in NSCLC specimens (n=24). Lines and boxes represent mean and SD, respectively. (**c**) Gating strategy to identify PD-1 subsets within peripheral blood CD8$^+$ T cells of healthy donors and within intratumoral T cells in NSCLC. (**d**) Effector cytokine secretion of sorted PD-1 subsets with and without anti-CD3/anti-CD28 stimulation

measured by bead-based immunoassay (mean and SEM of three donors). (**e**) Clonality of the TCR repertoire of PD-1^{T}, PD-1^{N} and PD-1^{-} TILs. Data from 11 NSCLC specimens are shown as box-and whisker-plots (the lines indicate median values, the boxes interquartile range (IQR) values and the whiskers 1.5IQR values as calculated by Tukey) (left). ***$P <$ 0.001 by one-way analysis of variance (ANOVA). The average relative abundance of the most frequent TCRβ clonotype, the second most frequent, the 3^{rd} to 30^{th} most frequent, and the remaining clonotypes are shown for all 11 donors (right). (**f**) Frequency of the 30 most abundant TCR sequences of the PD-1^{T} subset within PD-1^{T}, PD-1^{N} and PD-1^{-} populations. Shown are the mean percentage and standard deviation of all 11 donors. ***$P <$ 0.001, ****$P <$ 0.0001 by one-way ANOVA. (**g**) Expression of CD137 in PD-1 subgroups (n=24). Lines and boxes represent mean and SD, respectively. (**h**) Flow cytometry plot and quantification of pre-/postexpansion PD-1 expression and IFN-γ secretion of TILs expanded from the three sorted PD-1 subsets (n=3 NSCLC specimens). PD-1 MFI was analyzed within $CD3^{+}CD8^{+}$ cells from each expanded subset. Bar graphs indicate mean and SEM. ***$P <$ 0.001 by two-way ANOVA. (**i**) IFN-γ expression of expanded PD-1^{T}, PD-1^{N} and PD-1^{-} TILs from the eight donors upon co-culture with autologous digests. The difference with and without HLA class I blocking antibody is depicted for each individual donor (left) and T cell only and PMA/ionomycin controls are shown for all samples (mean and SD, right).

Europe PMC Funders Author Manuscripts

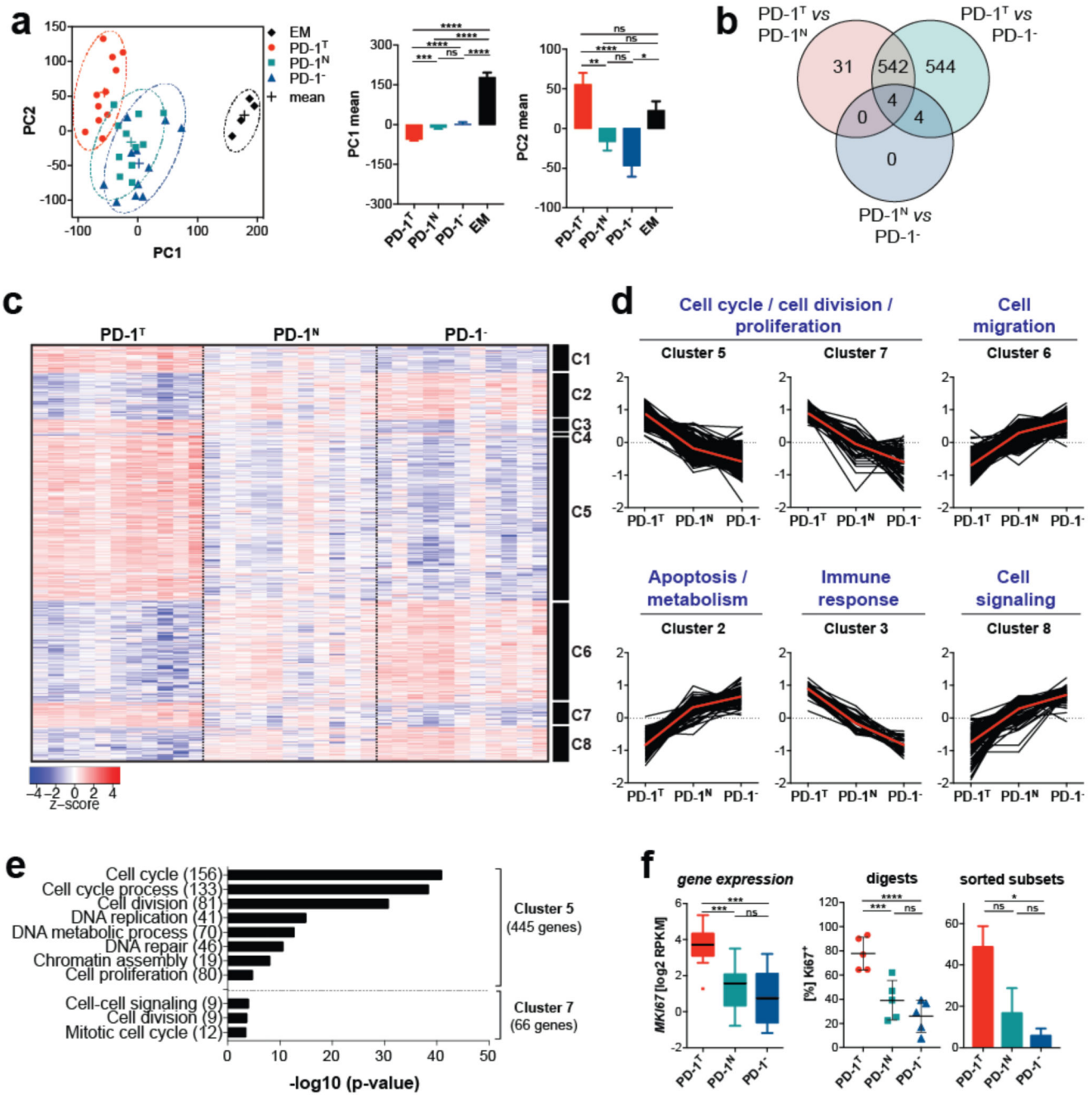

Figure 2. Gene expression profile of sorted PD-1^{T}, PD-1^{N} and PD-1^{-} TILs from NSCLC specimens.

(**a**) Principal component analysis (left) and bar plots for the means of the PC1 and PC2 values (right) for sorted PD-1^{T}, PD-1^{N}, PD-1^{-} TILs (n=11) and healthy donor effector memory (EM) T cells (n=4). Error bars represent the SEM. *P < 0.05, **P < 0.01, ***P < 0.001, ****P < 0.0001. (**b**) Significantly regulated genes between the three PD-1 subsets. Significance was determined as Benjamini-Hochberg FDR<0.01 and log2 fold change ≥1. (**c**) Clustering analysis for genes distinguishing PD-1^{T} from PD-1^{N} and PD-1^{-} subsets. (**d**)

Europe PMC Funders Author Manuscripts

Selected clusters showing up- or downregulation of key biological processes (Gene ontology (GO) terms). (**e**) Biological processes (GO terms) enriched in clusters 5 and 7. Numbers in parentheses indicate the number of genes within each GO term. (**f**) Increased expression of the proliferation marker Ki67 (*MKI67*) at the mRNA level (left, n=11), and at the protein level as assessed by intracellular staining of *ex vivo* tumor digests (n=5, middle) and sorted PD-1 subsets that were cultured for 48 hrs (n=3, right). The lines in the box-and whisker-plot indicate median values, the boxes IQR values and the whiskers 1.5IQR values as calculated by Tukey. The dot plots and bar graphs represent mean and SEM. *$P < 0.05$, ***$P < 0.001$, ****$P < 0.0001$ in (b), (c) and (d) by one-way ANOVA.

Europe PMC Funders Author Manuscripts

Europe PMC Funders Author Manuscripts

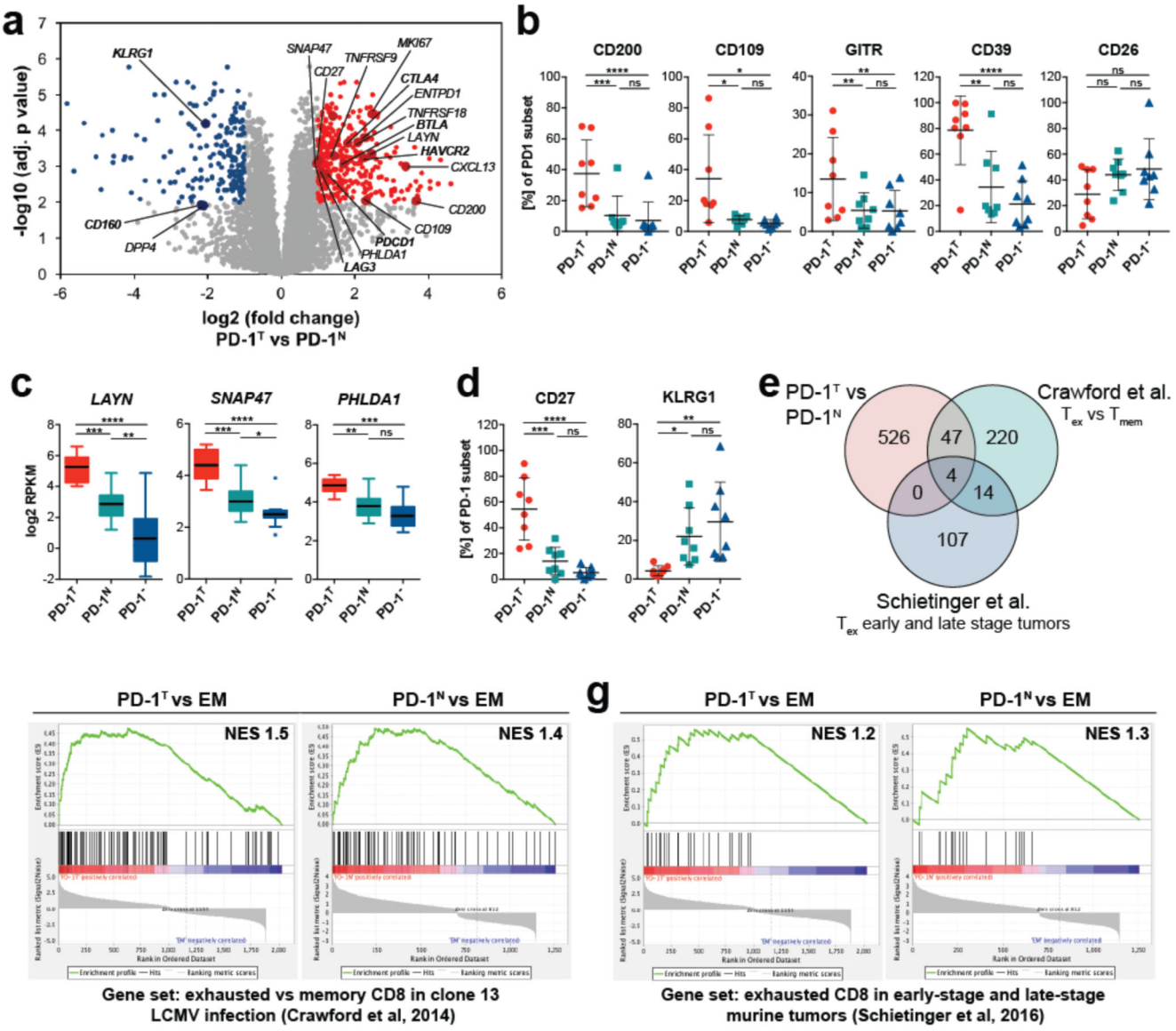

Figure 3. PD-1^{T} TILs show overexpression of inhibitory receptors, but display a key gene signature distinct from exhausted T cells in murine chronic infection and cancer.

(**a**) Volcano plot of up- or downregulated genes between PD-1^{T} and PD-1^{N} TILs, with a set of genes encoding inhibitory receptors and molecules involved in proliferation and differentiation annotated (n=11 tumor specimens). Significance was determined as Benjamini-Hochberg FDR<0.01 and log2 fold change ≥1. (**b**) Surface expression of indicated receptors on PD-1^{T}, PD-1^{N}, and PD-1^{-} gated TILs in tumor digests (n=8), as determined by flow cytometry. (**c**) Expression of the 'exhaustion genes' described in Zheng et al.27 in the indicated PD-1 subsets (n=11). The lines in the box-and whisker-plots indicate median values, the boxes IQR values and the whiskers 1.5IQR values as calculated by Tukey. (**d**) Surface expression of CD27 and KLRG1 on PD-1^{T}, PD-1^{N}, and PD-1^{-} gated TILs in tumor digests (n=8), as determined by flow cytometry. Each dot represents one patient. Bar graphs indicate mean and SEM. $^{**}P < 0.01$, $^{***}P < 0.001$, $^{****}P < 0.0001$ in

(b), (c) and (d) by one-way ANOVA. (**e**) Venn diagram comparing the overlap of the differentially expressed genes between PD-1^T and PD-1^N TILs with the genes derived from the chronic LCMV and the early/late-stage tumor signatures, respectively. (**f+g**) Gene set enrichment analysis (GSEA) of published data sets from exhausted T cells in (**f**) chronic murine LCMV infection (Crawford et al.) and (**g**) murine tumors (Schietinger et al.) within the gene signatures derived from the differently expressed genes between PD-1^T and EM T cells or PD-1^N and EM T cells (n=11 tumor specimens and 4 healthy donors). Statistical significance was determined by permutation testing with NES (normalized enrichment score).

Europe PMC Funders Author Manuscripts

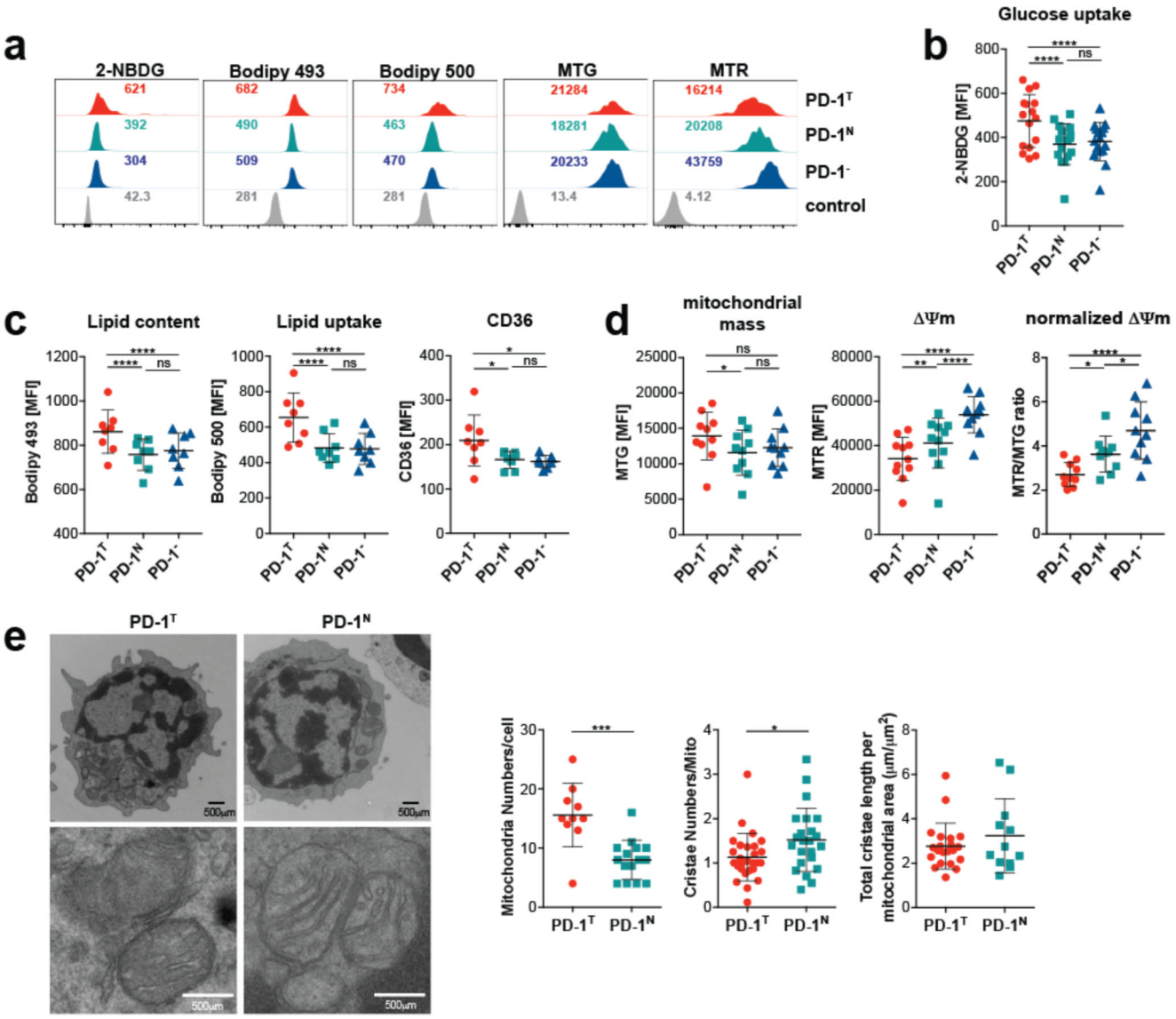

Figure 4. Alterations in glucose, lipid and mitochondrial metabolism in PD-1^{T} TILs.

(**a**) Representative histograms of metabolic parameters analyzed by flow cytometry in T cells of one donor (from n=3 independent experiments). (**b**) Glucose uptake (2-NBDG), (**c**) lipid content (Bodipy 493), uptake (Bodipy 500) and CD36 expression, and (**d**) mitochondrial mass (indicated by MTG), membrane potential ΔΨm (MTR), and normalized ΔΨm (MTR/MTG ratio) of PD-1^{T}, PD-1^{N} and PD-1^{-} gated TILs in 11 tumor digests. Shown are mean and SD. *P < 0.05, ****P < 0.0001 in (b), (c) and (d) by one-way ANOVA. (**e**) Representative electron micrographs of sorted PD-1^{T} and PD-1^{N} T cells and their randomly selected mitochondrial ultrastructures. Analysis of PD-1^{-} T cells or of independent biological replicates was precluded by limited cell numbers. Scale bars, 500 nm. Quantification of mitochondria numbers per cell, numbers of cristae in mitochondria and total cristae length normalized to the surface area of mitochondria using Image J. Sample identity was blinded to the analyser and at least 10 randomly selected TILs in each group

were quantified (PD-1^{T}: 10, 27, and 21 TILs; PD-1^{N}: 15, 23, and 12 TILs for each separate analysis). Data represent mean ± SD. *$P < 0.05$, ***$P < 0.001$ by Mann-Whitney test.

Europe PMC Funders Author Manuscripts

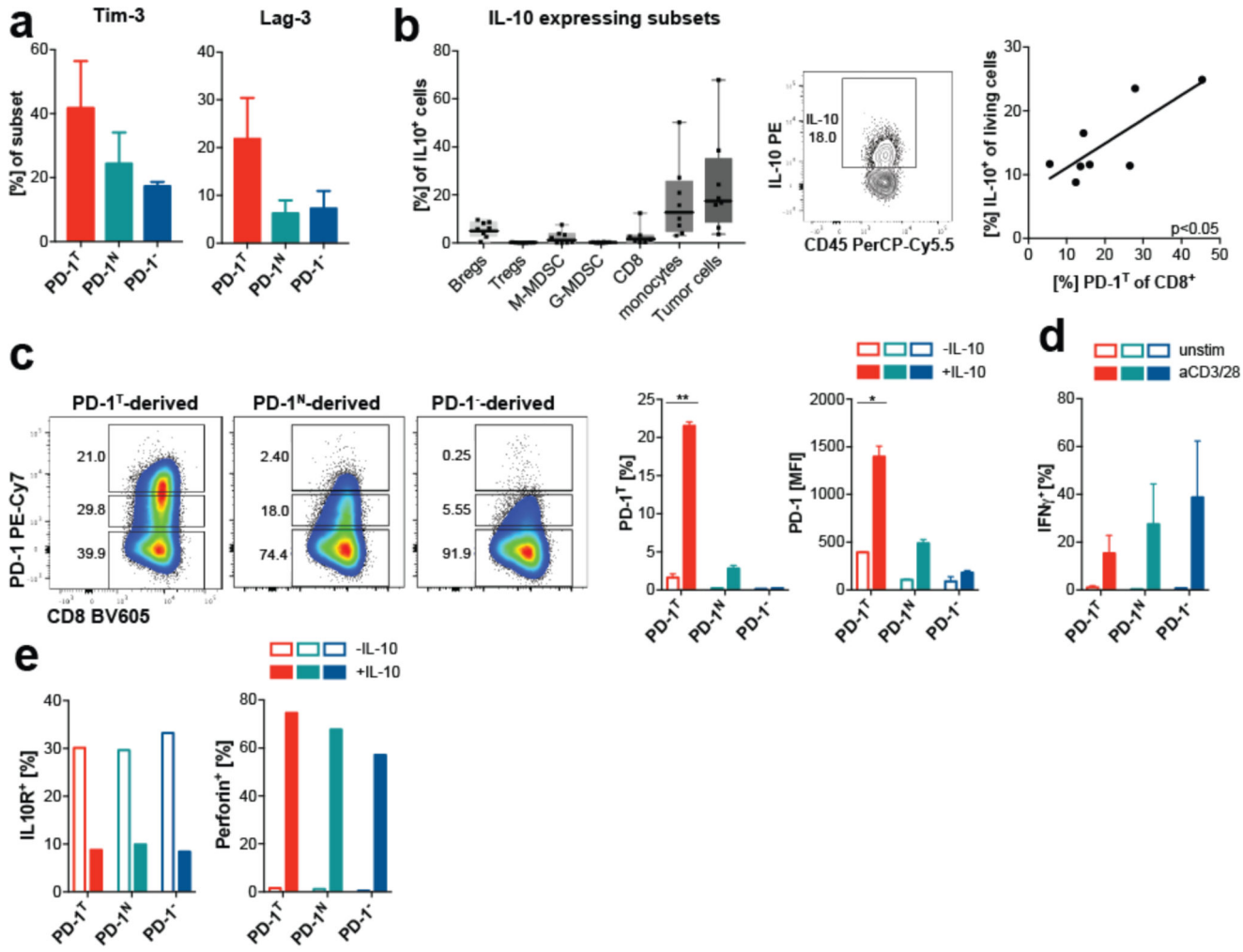

Figure 5. PD-1^{T} TILs display a fixed state of dysfunction.

(**a**) Expression of Tim-3 and Lag-3 in IL-2 expanded sorted TILs (n=3). Shown are mean and SEM. (**b**) IL-10 expression by indicated cell subsets in tumor digests and correlation of IL-10 expressing cells with the number of PD-1^{T} TILs (n=8). Lines in box-and-whisker-plots indicate median values, boxes indicate IQR values and whiskers minimum and maximum values. $R^2 = 0.61$ was calculated using linear regression analysis. (**c**) PD-1 upregulation in sorted TIL subsets after withdrawal of IL-2 and short-time IL-10 exposure (n=3). Bar graphs indicate mean and SEM. $*P < 0.05$, $**P < 0.01$ by one-way ANOVA. (**d**) IFN-γ production of IL-10 expanded PD-1^{T}, PD-1^{N}, PD-1^{-} sorted TILs (n=3). Bar graphs indicate mean and SEM. (**e**) IL10R and perforin expression in IL-2 expanded TIL subsets with and without IL-10 stimulation.

Europe PMC Funders Author Manuscripts

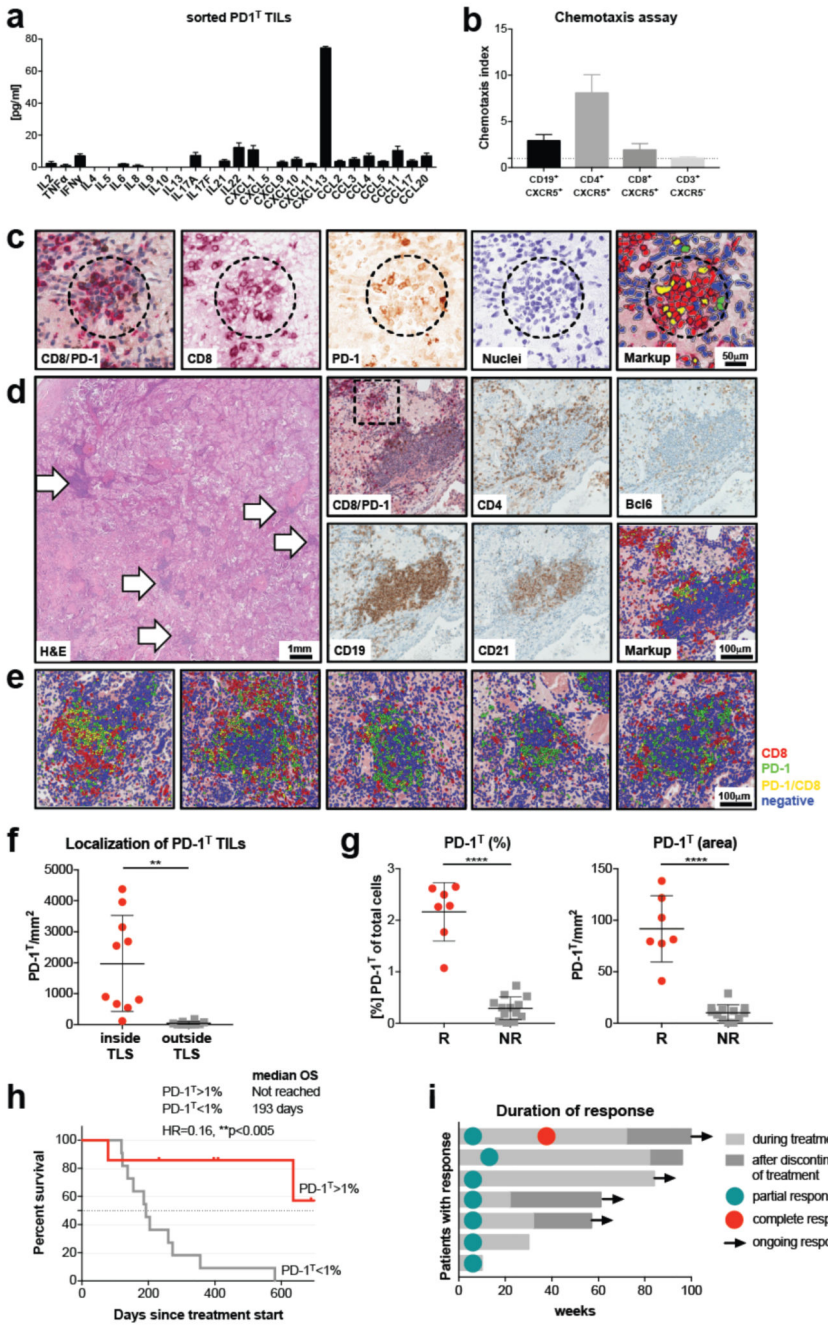

Figure 6. CXCL13 expression of PD-1^T TILs and predictive potential for response to PD-1 blockade.

(**a**) Expression of indicated inflammatory cytokines and chemokines in sorted PD-1^T TILs after 24 hrs of resting by bead-based immunoarray. Shown are mean and SEM of 3 donors. (**b**) Migration of peripheral blood CXCR5$^+$ CD8$^+$, CD4$^+$ and CD19$^+$ and CXCR5$^-$ CD3$^+$ immune cell subsets in response to CXCL13. Shown are the mean and SEM from three donors. (**c**) Digital markup images showing the color deconvolution of immunohistochemistry staining of CD8 (red) /PD-1 (brown) double positive cells. (**d**)

Immunohistochemical analysis of tertiary lymphoid structures (TLS) in lung cancer. Distribution of TLS in the tumor (large image, arrows indicate TLS, H&E). TLS show accumulation of CD8/PD-1^T double positive and $CD4^+$ T cells in the periphery of the follicular structure. Interspersed $Bcl6^+$ cells likely represent follicular helper T cells. A well-formed $CD21^+$ follicular dendritic cell network with strong accumulation of B cells is found in the center of the follicle. Digital markup image showing the color coding of $CD8^+$ (red), PD-1^+ (green), $CD8^+$PD-1^+ (yellow) and double negative (blue) cells in the TLS. (**e**) Digital markup images showing the localization of $CD8^+$, PD-1^+ and $CD8^+$PD-1^+ cells in five different NSCLC specimens. (**f**) Quantification of PD-1^T TILs localized within and outside of TLS in NSCLC specimens by digital image analysis (n=10). Shown are mean and SD. $^{**}P < 0.01$ by Mann-Whitney test. (**g**) Percentage of PD-1^T TILs per total cells or number of PD-1^T cells per mm^2 in responders (n=7) and non-responders (n=14) to PD-1 blockade. Shown are mean and SD. $^{****}P < 0.0001$ by Mann-Whitney test. (**h**) Overall survival of patients with tumors harboring more or less than 1% of PD-1^T cells (n=21). P value was determined by log-rank test. (**i**) Duration of response in the seven responding patients.